Journal of Power Sources 230 (2013) 130–137

Contents lists available at SciVerse ScienceDirect

Journal of Power Sources

journal homepage: www.elsevier.com/locate/jpowsour

Vanadium oxide nanowire – Graphene binder free nanocomposite paper electrodes for supercapacitors: A facile green approach

Sanjaya D. Perera [a], Anjalee D. Liyanage [a], Nour Nijem [b], John P. Ferraris [a], Yves J. Chabal [b], Kenneth J. Balkus Jr. [a,*]

[a] Department of Chemistry and the Alan G. MacDiarmid Nanotech Institute, 800 West Campbell Rd, University of Texas at Dallas, Richardson, TX 75080, USA
[b] Laboratory for Surface and Nanostructure Modification, Department of Material Science and Engineering, 800 West Campbell Rd, University of Texas Dallas, Richardson, TX 75080, USA

HIGHLIGHTS

- A facile green method was developed to grow VNWs on graphene surface.
- These VNWs are physically bonded on to the graphene surfaces.
- Flexible composite paper electrodes were prepared without using binders.
- The effect of the composition of VNWs in electrodes on electrochemical properties was studied.
- hGO–VNW paper electrodes show high power and energy densities.

GRAPHICAL ABSTRACT

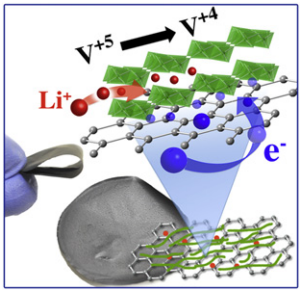

ARTICLE INFO

Article history:
Received 9 September 2012
Received in revised form
6 November 2012
Accepted 28 November 2012
Available online 13 December 2012

Keywords:
Graphene
Binder free composite paper electrodes
Flexible electrodes
Supercapacitors
Vanadium oxide nanowires

ABSTRACT

Vanadium oxide has attracted interest for energy storage applications due to its high theoretical capacitance and stable layered structure. The low electronic conductivity, of V_2O_5 necessitates combining with conducting materials, typically carbon. However combining with conductive carbon materials may require binders, which compromise the active surface. In this study, V_2O_5 nanowire (VNWs)–graphene composite flexible paper electrodes were prepared without using binders. Graphene introduces conductivity and electric double layer capacitance (EDLC) to the composite. Graphene sheets were prepared using an alkaline deoxygenation process (hGO), which is a *green* alternative to traditional hydrazine reduction. Coin cell type supercapacitors were assembled using the hGO–VNW paper electrodes as the anode and spectracarb fiber cloth as the cathode in a two-electrode cell configuration. Electrochemical studies for different compositions of VNWs on hGO are reported. The composite electrode hGO–VNW_{120}, showed balanced EDL and pseudocapacitance as well as an energy density of 38.8 Wh kg^{-1} at a power density of 455 W kg^{-1}. The maximum power density of 3.0 kW kg^{-1} was delivered at a constant current discharge rate of 5.5 A g^{-1}. The device prepared using hGO–VNW_{120} anode showed a specific capacitance of 80 F g^{-1}.

1. Introduction

Supercapacitors (*a.k.a.* ultracapacitors) are intermediate energy storage devices that can deliver much higher power densities than conventional batteries and higher energy densities than traditional capacitors [1–3]. They can be charged and discharged at high rates with long cycle life and low maintenance cost. Most importantly supercapacitors can be used in applications such as electric vehicles and high power applications which demand continuous high-energy within a short period of time. The major drawback of commercially available supercapacitors is the low energy density

* Corresponding author. Tel.: +1 972 883 2659; fax: +1 972 883 2925.
E-mail address: balkus@utdallas.edu (K.J. Balkus).

0378-7753/$ – see front matter © 2012 Elsevier B.V. All rights reserved.
http://dx.doi.org/10.1016/j.jpowsour.2012.11.118

(5–10 Wh kg^{-1}), which is much lower than Li ion (120–170 Wh kg^{-1}), lead acid (20–35 Wh kg^{-1}) and Ni metal hydride (40–100 Wh kg^{-1}) cells. [4] Despite the high energy density of batteries, the low power densities and low operational safety greatly limits the application of batteries in automotive industry and grid power storage systems. In contrast, supercapacitors can safely deliver as much energy as a battery, yet discharge in a short period of time.

Supercapacitors can be divided into two types, based on the mechanism of the charge storage, pseudocapacitance and electric double layer capacitance (EDLC). In EDLC the charges are stored at the electrode electrolyte interface, while for pseudocapacitors the charges are generated within the electrode due to a faradic reaction. Since the charges in EDLCs are stored at the electrode surface, they are readily accessible and resulting in high power densities. In contrast, pseudocapacitors generate a large number of charges due Faradic reactions. Therefore, electrochemical capacitors prepared using redox active materials exhibit higher specific capacitance than conventional EDLCs. Different types of transition metal oxides such as RuO_2, CuO, MnO_2, NiO, Co_3O_4, V_2O_5 have been shown a promise in pseudocapacitance [5–8]. For example ruthenium oxide (RuO_2) exhibits a high specific capacitance of 700 F g^{-1}, a wide potential window and reversible redox reactions [9,10]. Lee et al. reported high specific capacitance up to 1000 F g^{-1} based on the weight of hydrous RuO_2 [11]. However, the high cost of Ru based compounds limits the large-scale application in supercapacitor electrodes. Hence, much effort has been devoted to prepare a low cost alternative for RuO_2 that exhibits a high specific capacitance with a long cycle life. Nanostructured vanadium oxides have shown great promise for applications in energy storage. The redox-activity of vanadium oxides with multiple oxidation states (V^{+5}, V^{+4} and V^{+3}) is attractive for supercapacitors and Li ion batteries [12,13]. Moreover, V_2O_5 is a promising candidate for electrochemical capacitors due to the layered structure and ability to intercalate three Li^+ ions per V_2O_5 unit yielding a theoretical capacitance of ~400 mA h g^{-1} [14]. However, bulk V_2O_5 exhibits low electronic conductivity (10^{-2}–10^{-3} S cm^{-1}) and slow Li ion diffusion rates (D ~ 10^{-12} cm^{-2} s^{-1}), leading to low initial capacitance and rapid capacitance fading [15]. In contrast, nanostructured vanadium oxides have shown improved Li ion diffusion rates [16]. To date, wide range of nanostructures such as nanotubes, nanowires, nanobelts and nanorods of V_2O_5 have been prepared [17–24]. Also, freestanding flexible papers of V_2O_5 nanowires (VNW) can be prepared by vacuum filtration. Unfortunately, due to the low electronic conductivity of the VNWs conducting materials such as carbon materials must be added. Liu et al. have prepared reduced graphene oxide (rGO)–VNW composite electrodes for Li ion battery cathodes and exhibited promising performance for Li ion storage [25]. Rui and co-workers deposited polycrystalline V_2O_5 spheres on rGO sheets and demonstrated their high capacitance capabilities in Li ion batteries [26].

Typically, the preparation of VNW/Carbon composite electrodes generally requires a binder. These binders significantly reduce the active surface area of the electrodes available for ion diffusion and charge transfer. Moreover, the additional weight associated with the binders lowers the power and energy density that is based on the mass. Therefore, there is a great interest in preparing V_2O_5/carbon composites without using binders. Different methodologies have been reported for growing or depositing of V_2O_5 on carbon substrates such as on carbon fiber fabrics and carbon nanotubes (CNTs) [16,18]. Carbon nanotubes have shown great promise for supercapacitors. The conductivity and the ability to form freestanding papers make them an ideal candidate for binder free composite electrodes. Different types of metal oxides including V_2O_5 have been used to prepare composites with CNTs [26–28]. Previously we reported binder-free V_2O_5 nanowire–carbon nanotube composite paper electrodes, which exhibit high energy and power densities [16]. Fang et al. observed fast and reversible surface redox reduction in V_2O_5 dispersed on CNTs [19]. In these composite electrodes, the CNTs improve the overall electronic conductivity and charge transfer. Unfortunately the high manufacturing cost and impurities present in CNTs samples limits the use of CNTs in large-scale industrial applications.

Graphene has become an attractive low cost alternative for CNTs. Composites prepared using graphene has shown a great promise in energy storage as well as catalysis and solar cells [29–35]. The high surface area graphene layers could serve as a support for metal oxide nanostructures. The metal oxides deposited on the surface of graphene keep graphene layers well separated from strong van der Waals interactions during preparation. Moreover, vacuum filtration of graphene dispersion yields binder free flexible thin membranes, which could be utilized in electrodes [36,37].

Single sheets or few layers of graphene sheets are typically prepared via oxidation to graphene oxide followed by reduction. Typically, graphene oxide requires chemical or thermal treatment to be reduced back to graphene. Chemical reduction of graphene oxides is achieved by reducing agents such as hydrazine, alcohols and amines [38–41]. Recently we developed a green method to deoxygenate GO to yield highly quality conducting graphene, which exhibited good electrochemical and capacitive properties [36]. VNWs have been prepared on deoxygenated GO (hGO) and self assembled to form freestanding flexible paper electrodes for supercapacitors. Coin cells were prepared with the hybrid composite paper electrodes with anode and carbon fiber cloth as the cathode. Then, correlation between the composition of VNWs/hGO and the electrochemical properties were studied to optimize the specific capacitance. These composite electrodes with optimum composition of hGO and VNW exhibited promising energy and power density in coin cell type supercapacitors.

2. Experimental section

2.1. Materials

All reagents were used without further purification. Vanadium (V) oxytriisopropoxide (99%) was purchased from Sigma–Aldrich. Pluronic® P123 Surfactant was obtained from BASF corporation. Graphite was purchased from Sigma–Aldrich. High surface area carbon fabric (Spectracarb 2225) and carbon fiber sheet (Spectracarb 2250A) were purchased from Engineered fiber technology (Shelton, CT). Lithium bis(trifluoromethanesulfonamide) (LiTFSI) was obtained from TCI America. A Teflon film (Gore Company) was used as the separator between two electrodes. All solvents were used as received. Typical coin cell package (CR2032) was used to assemble all coin cell type supercapacitors.

2.2. Synthesis of V_2O_5 nanowires (VNWs) on alkaline deoxygenated graphene oxide (hGO)

hGO was prepared according to the procedure found in elsewhere [36]. 10 ml of as prepared hGO dispersion (1 mg ml^{-1}), 5 ml of ethanol and 0.15 mg of Pluronic® P123 was stirred in a vial for 15 min. Different volumes of vanadium (V) oxytriisopropoxide (VOTIP) was slowly introduced to the mixture drop wise. The mixture was stirred at room temperature for 2 h, transferred to a Teflon® lined autoclave and heated at 120 °C for 24 h. Finally, the composite dispersions were suction filtered using Nylon filter paper (Nylon 66, 0.45 μm) and washed with excess DI water. The papers were allowed to dry at room temperature and then peeled

off the filter paper as a flexible freestanding paper. Volume of VOTIP was varied from 20, 40, 60, 120 and 200 μl to prepare composite papers hGO–VNW_{20}, hGO–VNW_{40}, hGO–VNW_{60}, hGO–$VNW1_{20}$ and hGO–VNW_{200}.

2.3. Synthesis of V_2O_5 nanowires (VNWs) on hydrazine reduced graphene oxide (rGO)

rGO was prepared according to the procedure previously reported [36]. 10 ml of as prepared rGO dispersion (1 mg ml^{-1}), 5 ml of ethanol and 0.15 mg of Pluronic® P123 was stirred in a vial for 15 min. The mixture was stirred at room temperature for 2 h, transferred to a Teflon® lined autoclave and heated at 120 °C for 24 h. Similar to the procedure described earlier was followed to prepare rGO–VNW composite freestanding paper.

2.4. Coin cell type supercapacitor assemble

In the coin cell packaging (CR2032) as described in elsewhere, the composite paper was the anode and the carbon fiber cloth (Spectracarb 2225) was the cathode, which were separated by Teflon® film [16,18,36]. The electrolyte, 1 M Lithium bis(trifluoromethanesulfonimide) (LiTFSI) in acetonitrile, was introduced to each electrode and sealed in coin cell using coin cell crimper by pressing at 1500 psi.

2.5. Characterization

Scanning electron microscope (SEM) and Transmission electron microscope (TEM) images were acquired using a Leo 1530 VP field emission electron microscope and a JEOL JEM-2100 TEM at 200 kV (JEOL Co. Ltd.). X-ray powder diffraction (XRD) patterns were obtained using a Rigaku Ultima IV diffractometer (Cu Kα radiation). X-ray Photoelectron Spectroscopy (XPS) measurements were recorded *ex-situ*, using a Perkin Elmer PHI System. The photoelectrons are excited using monochromatic Al K_α radiation ($h\nu = 1486.6$ eV) and the spectra are acquired with 45° emission angle, using 0.125 eV step size and a pass energy of 29.35 eV in the hemispherical analyzer. The nominal pressure in the analysis chamber is 3×10^{-9} Torr. Cyclic voltammograms (CV) and galvanostatic charge/discharge curves (CDC) were recorded using Arbin battery testing system (BT2000) in the voltage window of 2 V. Electrochemical impedance spectroscopy (EIS) measurements were performed on computer controlled EG&G Princeton Applied Research potentiostat/galvanostat (model 273A).

3. Results and discussion

3.1. Morphology of hGO–VNW paper electrodes

Fig. 1a shows a graphical scheme for the formation of V_2O_5 nanowires on hGO sheets. In our previous study on hGO, we reported the presence of ~20% oxygen functional groups [37]. During the hydrothermal treatment, V^{+5} ions bind to these oxygen functional groups and subsequently grow into the V_2O_5 nanowires. It has been shown that the addition of surfactant (P123) can control the morphology of the V_2O_5 nanowires [21]. The surfactant and ethanol can also partially reduce the V^{+5} to V^{+4}. Typical morphology of the hGO sheets before the hydrothermal synthesis of VNWs is shown in Fig. 1b. Inset image shows the cross sectional SEM image of the freestanding hGO electrode. As previously reported, hGO sheets tend to restack to form layered morphology with a thickness of ~10 μm [36]. These graphene layers with wrinkles on the surface and provide high surface area substrate for growing the VNWs. In order to prepare a series of hGO–VNW composites, different volume of vanadium (V) oxytriisopropoxide (VOTIP) was used as the starting material varying from 20, 40, 60, 120 and 200 μl, which denotes hGO–VNW_{20}, hGO–VNW_{40}, hGO–VNW_{60}, hGO–$VNW1_{20}$ and hGO–VNW_{200}.

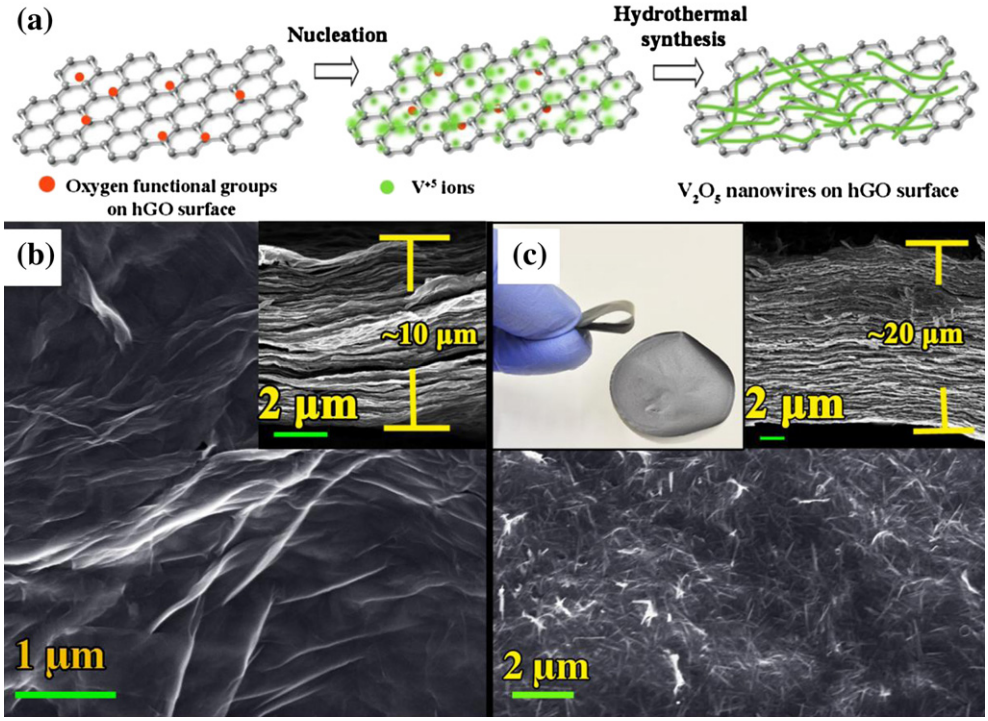

Fig. 1. (a) A schematic diagram showing the formation of hGO–VNW composite. (b) SEM micrographs of the surface and cross section of the hGO paper (inset). (c) Surface morphology of hGO–VNW_{120} composite paper. Inset shows a digital image and cross sectional SEM image of the flexible freestanding hGO–VNW_{120} paper.

The as prepared V_2O_5 nanowires are grown on the surfaces of the graphene sheets as shown in Fig. 1c. The digital image of the hGO–VNW_{120} freestanding, flexible paper obtained after vacuum filtration and cross sectional SEM image are shown in Fig. 1c inset. The loosely stacked layered structure provides porosity and facilitates the ion diffusion along the sheets. The thickness of the composite paper electrode is almost as twice as the thickness of the hGO electrodes (~20 μm), suggesting that the VNWs act as spacers between layers. Moreover, the randomly oriented VNWs on hGO sheets create a microporous structure for better ion diffusion within the electrode. The VNWs also significantly prevent the graphene sheets from restacking. Fig. 2a shows a TEM image of an hGO sheet. The shown in Fig. 2b shows a Single layer or few layers of graphene with an intimate network of V_2O_5 nanowires (Fig. 2b). The as synthesized V_2O_5 nanowires have a diameter of ~40 nm on the surfaces of the graphene sheets. The VNWs are similar in size to nanowires previously prepared on CNTs.

3.2. Characterization of hGO–VNW composite papers

The X-ray diffraction pattern of the hGO–VNW composite shown in Fig. 3a exhibits characteristic peaks at (001), (002), (201), (110), (004), (011) and (005) corresponding to the V_2O_5 phase [42]. These diffraction peaks can be indexed as the $V_2O_5.nH_2O$ monoclinic phase [43]. The low oxidation states of vanadium oxide in $V_2O_5.nH_2O$ is balanced by positive ions (H^+) The XRD pattern of hGO typically shows a broad band around 26° due to the (002). This could overlap with (201) and (110) reflections of V_2O_5 in the XRD pattern of the composite. The X-ray photoelectron spectra (XPS) of hGO–VNW_{120} further reveal the partial reduction of V^{+5} to V^{+4} (Fig. 3b). The peak at 517.6 eV is attributed to the $V2p_{3/2}$ electrons of vanadium +5 oxidation state. Deconvolution of this peak shows a peak at 516.3 eV, which corresponds to the +4 oxidation state [16]. Based on the XPS spectra the calculated molar ratio of V^{+4}/V^{+5} was ~0.58. This is much higher than previously observed for VNWs grown in the absence of graphene but may reflect the use of ethanol solvent, reducing agent, in the present study [18,21]. Our previous studies on hGO for supercapacitor electrodes showed a dramatic decrease in C–O bonding after alkaline deoxygenation of GO, which is similar to the hydrazine reduction [36]. The C 1s peak at 284 eV OF XPS shows the presence of C–C and deconvolution reveals the oxygen functional groups in hGO. Compared to hGO, the intensity of the C–O (~286 eV) peak is higher than that of hGO peak intensity reported earlier [36]. This may be due to the vanadium bound to hGO through a C–O bond. Based on the XPS studies, the estimated V:C atomic ratio of the composite electrode was 0.16:1.

The room temperature Raman spectrum of the hGO–VNW_{120} composite is shown in Fig. 4a. The vibrational Raman modes can be characterized on the basis of five-fold coordination of vanadium with oxygen. The strong peak at 137 cm^{-1} is due to the skeleton bending vibrations of the V–O–V bond [44]. The peaks at 505 cm^{-1} and 680 cm^{-1} are attributed to the bending vibrations of V–O–V (bridging doubly coordinated oxygen) and V_3–O (triply coordinated oxygen) bonds, respectively [45]. The peak centred at 998 cm^{-1} corresponds to the in-phase stretching vibrational mode related to the apical vanadium oxygen bond V=O [46]. The angle bending modes can be represented in the 200–500 cm^{-1} region. Raman bends at 400 and 276 cm^{-1} correspond to the x and y displacements of O_1 atoms, while the line at 183 cm^{-1} originates from A_g and B_{2g} modes [47]. In addition to the bands corresponding to the V_2O_5, the characteristic D and G bands of graphene appears 1320 and 1590 cm^{-1} respectively (Fig. 4a, inset). The D band associated with the sp^3 carbons while the G band arises from the sp^2 carbons of the graphene lattice. Based on the Raman spectrum acquired in the range of 1100–1800 cm^{-1}, the intensity of the G band is higher that that of D band suggesting the graphene lattice consists of more sp^2 carbons. Moreover, the intensity ratio of D/G band is a measure of the sp^2 domain size, the lower the I_D/I_G ratio higher the sp^2 domain size. It is important to have large conducting domains to effectively shuttle electrons between VNWs and graphene. Previous we reported that hGO prepared using the alkaline deoxygenation of graphene oxide exhibits a larger domain size of graphite microcrystals than that of hydrazine reduced graphene oxide [36]. In the current study, the calculated I_D/I_G was ~0.8, which is comparable to the values we obtained in previous reports [31,36]. In addition to the intensity ratio of D/G bands, the G band position of graphene provides evidence for physiochemical interaction between graphene layers and VNWs. The G band of hGO–VNW_{120} composite appeared at higher wave number than that of hGO (~1600 cm^{-1}) (Fig. 4b). Tsukamoto et al. reported the effect of the surface chemistry of substrates on Raman spectra of graphene using different substrates [48,49]. The blue shift observed in the G band of the composite (~10 cm^{-1}) is attributed to the chemical doping and the surface interaction of graphene–V_2O_5 interface. Based on Raman studies, the VNWs are physically attached to the hGO sheets and introduce conductivity within the composite electrode providing pathways for charge transfer reactions.

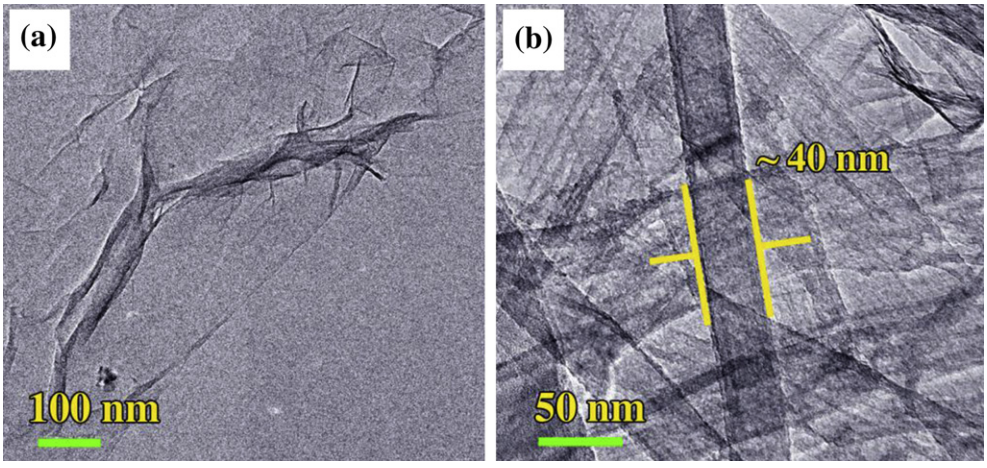

Fig. 2. TEM images of (a) an hGO sheet and (b) an hGO–VNW_{120} composite.

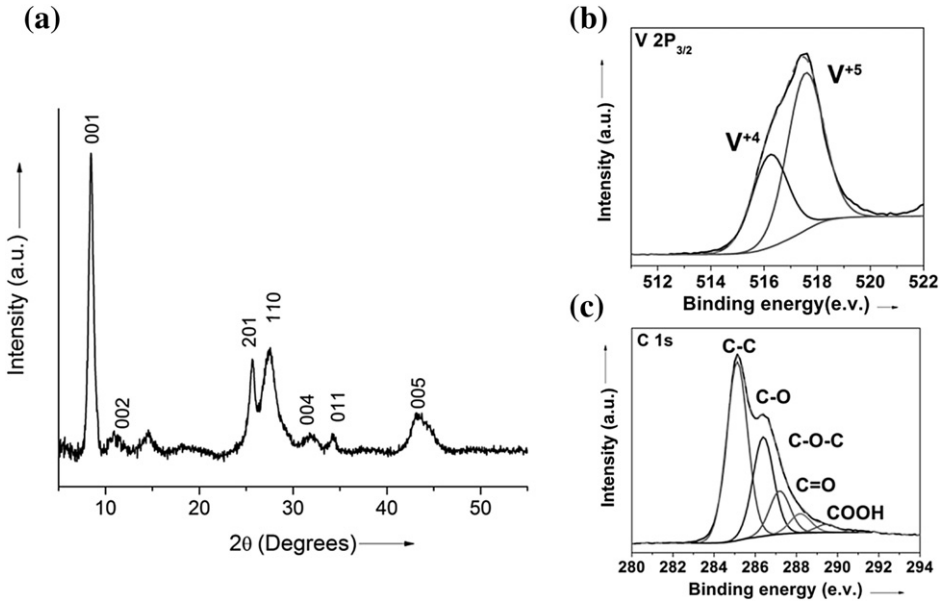

Fig. 3. (a) XRD pattern of hGO–VNW$_{120}$ composite paper. XPS spectra of (b) V2p$_{3/2}$ electrons and (c) C 1s electrons. XPS spectra of C 1s electrons corresponds to hGO was previously reported elsewhere [35].

3.3. Electrochemical characterization of hGO–VNW paper electrodes

The layered structure of V_2O_5 structure allows Li ions to be reversibly intercalated according to Equation (1) in the potential range between 2.5 V and 3.5 V versus Li/Li$^+$ [50].

$$V_2O_5 + xLi^+ + xe^- \leftrightarrow Li_x^+V_{2-x}^{5+}V_x^{4+}O_5^{2-} \quad (1)$$

During the charge cycle nearly 3 Li$^+$ ions per V_2O_5 molecular unit is intercalated leading to a partial reduction of V^{+5} to V^{+4}. While VNWs generates pseudocapacitance, the graphene sheets effectively create conducting paths for the electrons. Graphene also generates EDLC, thus improving the overall capacitance of the composite electrode. Additionally, the pseudocapacitance and EDLC should be balanced in the electrodes to achieve the optimum capacitive behavior. We previously reported that different compositions of V_2O_5 nanowires in a CNT matrix could be optimized to balance the pseudocapacitance and EDLC [18]. The presence of excess VNWs in the composites leads to higher pseudocapacitance than that of optimum compositions.

In order to analyze the electrochemical behavior of the hGO–VNW composite paper electrodes, CR2032 type coin cell asymmetric supercapacitors (two-electrode systems) were assembled. During the discharge and charge cycles V^{+4} presence in the hGO–VNW anode oxidizes to +5 and reduces to lower oxidation states respectively. Fig. 5 shows the cyclic voltammograms acquired for different hGO–VNW compositions in the potential window of 2 V using LiTFSI in acetonitrile as the electrolyte. These results indicate that a different ratio of hGO to VNW results in different electrochemical properties. It can be argued that there are three main processes occur at the interfaces between the electrolyte, hGO and VNWs. First electron transfer along the graphene sheets (electronic conductivity), second redox reactions that occur within the V_2O_5 layers upon insertion of Li ions and third, EDLC formation at the interface of the hGO and electrolyte. Therefore to have both high capacitance and good energy, power performance, all these three factors need to be balanced so that the ideal capacitive properties can be attained.

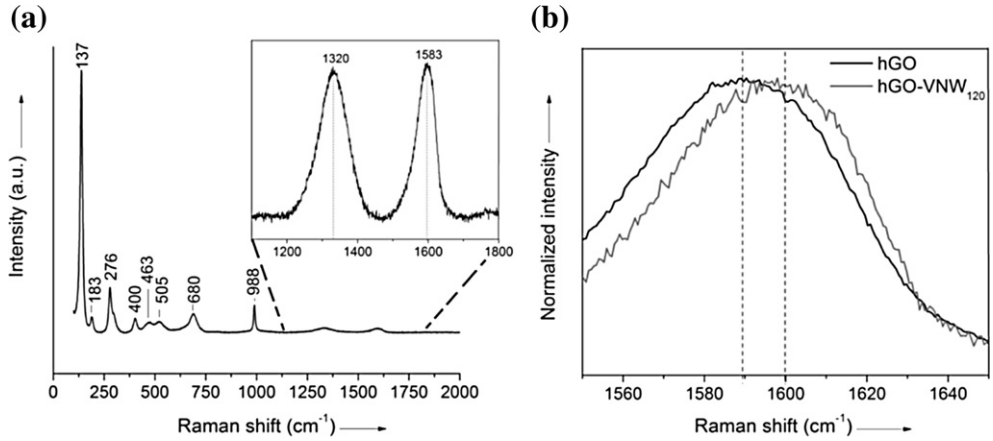

Fig. 4. (a) Raman spectrum of hGO–VNW$_{120}$ composite paper (Figure a inset). D and G bands of hGO in the composite. (b) Comparison of the G band of hGO and hGO–VNW$_{120}$ composite.

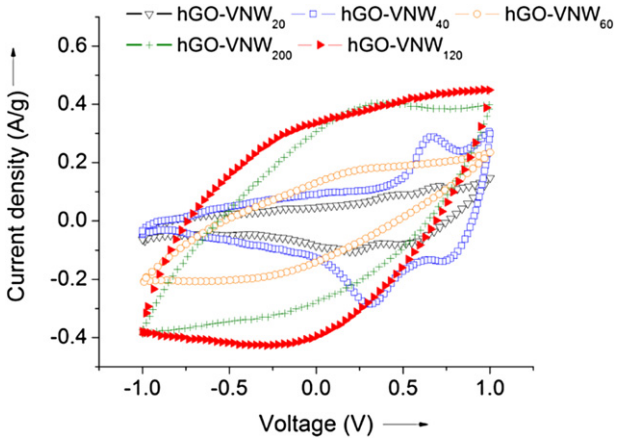

Fig. 5. Cyclic voltammograms of hGO–VNW composite papers with different VNW compositions (acquired at a scan rate of 20 mV s^{-1}).

The composites having higher amounts of hGO (hGO–VNW_{20} and hGO–VNW_{40}) exhibit clear cathodic and anodic peaks due to vanadium oxidation and reduction. Moreover, the current output of the oxidation and reduction peaks suggests that reversible insertion and de-insertion of Li ions between the V_2O_5 layers occurs. The compared to the hGO–VNW_{20} and hGO–VNW_{40}, composites having higher amounts of V_2O_5 (hGO–VNW_{60}, hGO–VNW_{120} and hGO–VNW_{200}) exhibit broad redox peaks. The degree of conductivity and EDLC of the electrode is mainly controlled by the amount of hGO in the electrode. Thus, composites having higher amounts of hGO create large number of conducting paths along the graphene sheets. The lower resistance to the electrons increases the reversible electron transfer rates during the charge and discharge process. This argument is in agreement with the presence of resolved anodic and cathodic peaks of the composites having higher contents of hGO. However, the composite electrode that has the highest content of V_2O_5 (hGO–VNW_{200}) starts slightly deviate from the capacitive behavior.

To further explore the performance of the hGO–VNW_{120} electrode, CV diagrams of the composite electrode were recorded at different voltage scan rates (Fig. 6a). The CVs in Fig. 6a are nearly rectangular and exhibit balanced capacitive performance over the voltage sweep rates of 5–30 mV s^{-1}. Moreover, the absence of redox peaks in all voltammograms at different scan rates indicates that the supercapacitors are charged and discharged at a pseudo-constant rate over the entire voltammetric cycles [51]. Compared to the other studies on V_2O_5 based electrodes, hGO–VNW_{120} composite electrode generates higher current densities in a larger voltage window than aqueous electrolytes [24,52]. In contrast to aqueous electrolytes, the organic electrolyte used in this extends the accessible voltage window up to 2 V [53]. To evaluate the electrochemical behavior of the hGO in the electrode, a CV measurement of the hGO electrode as the anode was performed at a 25 mV s^{-1} scan rate. As shown in Fig. 6b, Compared to the hGO electrode the area under the CV corresponding to the hGO–VNW composite electrode is much smaller, suggesting that the presence of VNWs significantly enhances the electrode performance. Compared to the hGO electrode, where EDL dominates the overall capacitance, higher current output of hGO–VNW_{120} electrode is mainly due to the generation of large number of charges by the redox active V_2O_5.

As shown in Fig. 6c, the charge–discharge behavior of hGO–VNW_{120} composite electrode was characterized under Galvanostatic conditions. The Galvanostatic charge–discharge curves were

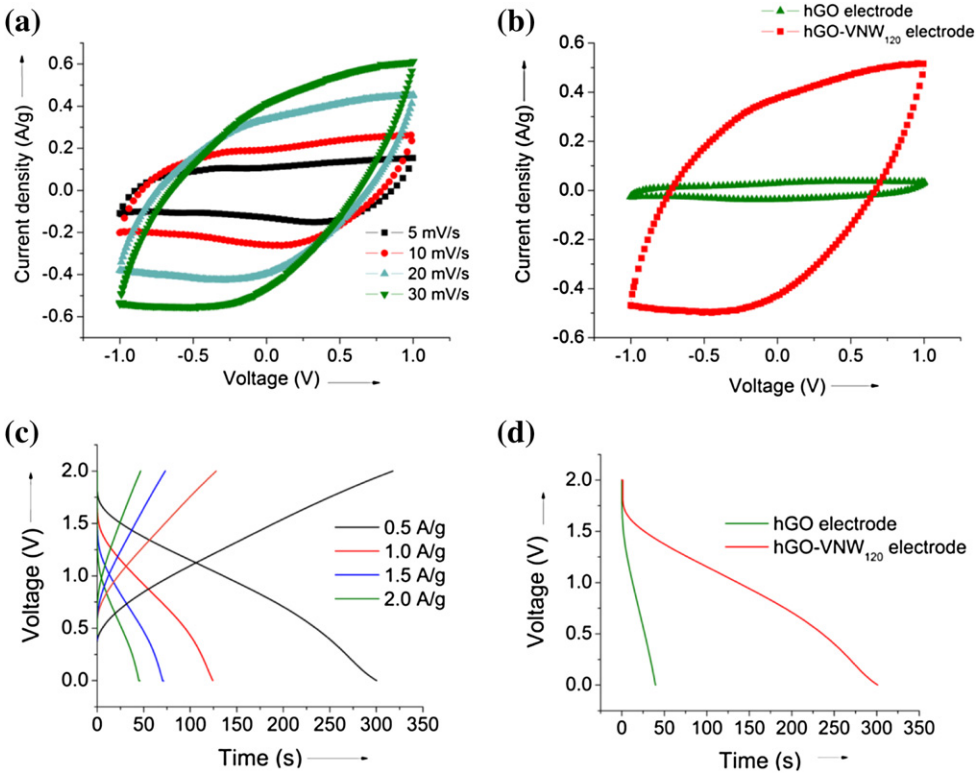

Fig. 6. (a) Cyclic voltammogram of hGO–VNW_{120} at scan rates of 5, 10, 20 and 30 mV s^{-1} and (b) Comparison of the CV diagrams of hGO–VNW_{120} and hGO electrodes. (c) Galvanostatic charge–discharge profiles of hGO–VNW_{120} at different current densities and (d) Comparison of discharge profiles at a constant current density of 0.5 A g^{-1}.

recorded at different constant current densities (0.5–2.0 A g^{-1}). The charge–discharge profiles exhibit a nearly linear rate of discharge indicates the balanced EDL and pseudocapacitance components presence under both high and low constant current densities. Compared to hGO electrode, the discharging time of hGO–VNW_{120} composite at constant current density of 0.5 A g^{-1} was significantly increased, suggesting that combination of VNWs and hGO offers a larger charge capacity, which was consistent with the CV profiles (Fig. 6d). Based on Galvanostatic discharge curves, energy, power densities and specific capacitance were calculated based on the total weight of the anode and cathode. The energy and power densities for composite papers were calculated according to the equation:

$$E = (I \times \Delta t \times \Delta V)/(2 \times m) \text{ and } P = E/\Delta t$$

where I is the constant discharge current, Δt is the discharge time, ΔV is the voltage difference after the voltage drop and m is the total mass of both electrodes (carbon fiber electrode and the composite paper electrode). The hGO–VNW_{120} composite electrode shows an energy density of 38.8 Wh kg^{-1} at 0.5 A g^{-1} discharge rate with a considerable power density of 465 W kg^{-1}. The energy and power densities of hGO–VNW electrode are higher than that of reported value of CNT/V_2O_5 composites [20]. This composite electrode can deliver a maximum power density of 3.0 kW kg^{-1} at a constant current density of 5.5 A g^{-1}. In contrast to hGO–VNW_{120}, Even though hGO electrode delivers nearly equal power density (455 W kg^{-1}) at a 0.5 A g^{-1} of constant current density, the calculated energy density at this rate was only about 5 Wh kg^{-1}. In contrast to hGO, the presence of VNWs increases the energy density of the hGO–VNW_{120} electrode about four times than that of hGO electrode. The improved energy density of hGO–VNW composite represents that under the same constant current discharge conditions, the VNWs on the hGO sheets possesses redox reactions, which generates large number of charges. The specific capacitance (C_{sp}) of the electrodes was calculated using the equation:

$$C_{sp} = (I \times \Delta t)/(m \times \Delta V).$$

Furthermore, specific capacitance of the supercapacitor fabricated with hGO–VNW_{120} yields a specific capacitance of 80 F g^{-1}, which in consistence with the CV and discharge profiles. The electrochemical properties of hGO–VNW_{120} were further compared with rGO–VNW_{120}. Fig. S1 shows the capacitive behavior of rGO–VNW_{120} electrodes, which closely resembles the balanced EDLC and pseudocapacitive properties. The energy density of rGO–VNW_{120} electrode was ~24 Wh kg^{-1}. The specific capacity of the device calculated at this current density was ~47 F g^{-1}. Compared to the hGO, It was previously observed that the lower energy density and specific capacity of rGO in organic electrolytes. This can be attributed to the presence of larger sp^2 domains on hGO than that of rGO [36]. These domains can effectively transfer electrons while defected carbons (sp^3) provide physical contact with VNWs.

In addition to the large number of electron and ion percolation paths and numerous suitable pores for efficient ion access, the resistive components associate with electrodes critically influences the excellent electrode performance. To evaluate the resistive components, the electrochemical impedance spectroscopy (EIS) measurements were performed on both hGO and hGO–VNW_{120} composite electrodes. The EIS measurements in Fig. 7a indicate both electrodes display ideal capacitive behavior with a semicircle at high-medium frequency and an inclined line at low frequency, which corresponds to charge transfer and diffusion respectively [18,54]. The first intersection point on the real axis of the impedance spectrum in the high frequency region represents the total of electrolyte (R_s), electrodes (R_e) and the contact (R_c) resistance between the electrode and current collector. The second intersection point on the real axis at medium frequency is associated with the interfacial contact capacitance (C_c) and charge transfer resistance (R_{ch}). Compared to hGO electrode, the smaller diameter of the semicircle in the impedance plot corresponds to the hGO–VNW_{120} electrode is an indication of the low charge transfer resistance. The recorded charge transfer resistances of hGO–VNW_{120} and hGO electrode are 7.5 Ω and 11.3 Ω respectively. The lower charge transfer resistance of the composite electrode is attributed to the effective ion diffusion and transfer within VNWs and micro-pore structure of the hierarchical network of VNWs on hGO sheets. Thus, the synergistic contribution of hGO and VNWs with improved charge transfer across the V_2O_5 layers and along the surfaces of hGO layers introduces superior electrochemical properties to hGO–VNW_{120} composite. Cycling stability of the hGO–VNW_{120} was evaluated by charging and discharging over 70 cycles. The retention of the specific capacitance against the cycle number is shown in Fig. 7b. After 20th cycle ~80% of the specific capacitance was retained while after 50th cycle ~70% of the capacitance was retained and stabilized over the next cycles. The initial drop of the retention of the specific capacitance may be due to the dilution of Li ions in the electrolyte medium. Unlike in Li ion batteries, where Li foil serves as the Li ion source, in this study the primary Li ion

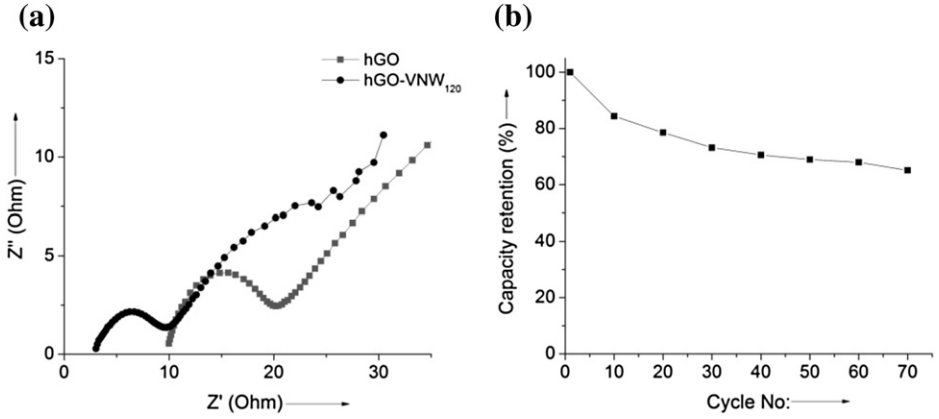

Fig. 7. (a) Electrochemical impedance spectra of hGO and hGO–VNW_{120} electrodes collected at open circuit voltage of 0.5 V. (b) Capacitance retention of hGO–VNW_{120} over 70 charge/discharge cycles.

source is the LiTFSI. Upon the discharge cycle Li ions form the electrolytes can be intercalated to form LiC_6 the carbon fiber cathode, which could lead to the dilution of Li ions during initial discharge cycles [36,55]. However, the stability of the VNWs on hGO is comparable to the previous reports on vanadium oxide based electrodes [16,51]. Thus, binder-free approach to fabricate freestanding flexible hGO–VNW composite electrodes with high energy and power performance with cycling stability would be much beneficial in low cost lightweight applications, which require high energy and power.

4. Conclusion

In conclusion, we were able to grow V_2O_5 nanowires (VNWs) on graphene sheets. Graphene sheets were prepared using alkaline deoxygenation process, which is a *green* alternative to hydrazine reduced graphene. Facile one-pot in-situ synthesis scheme for growing VNWs on hGO layers was developed. Binder free flexible graphene–V_2O_5 nanowire composite paper electrodes were prepared by vacuum filtration method. As prepared hGO–VNW electrode served as the anode while spectracarb fiber cloth as the cathode in two-electrode cell configuration. In order to investigate optimum composition of the graphene and VNWs, composite paper electrodes were prepared by varying the amounts of VNWs. The hGO–VNW_{120} composite showed the balanced EDLC and pseudo-capacitance, which confirmed by CV and Galvanostatic discharge profiles. As prepared hGO–VNW_{120} paper electrode delivered the highest energy density of 38.8 Wh kg^{-1} at a constant discharge current of 0.5 A g^{-1} while maintaining a power density of 465 W kg^{-1}. Moreover, highest specific capacitance of 80 F g^{-1} for the device calculated at this point clearly indicates that the graphene–V_2O_5 nanowire composite electrode is capable of store and delivers charges effectively for high-energy demand applications.

Acknowledgements

We would like to acknowledge the Department of Energy (DE-EE004186) for financial support.

Appendix A. Supplementary data

Supplementary data related to this article can be found at http://dx.doi.org/10.1016/j.jpowsour.2012.11.118.

References

[1] M. Winter, R.J. Brodd, Chem. Rev. 104 (2004) 4245.
[2] A. Aricò, P. Bruce, B. Scrosati, J.-M. arascon, V. Schalkwijk, Nat. Mater. 4 (2005) 366.
[3] C. Liu, F. Li, M. Lai-Peng, H.-M. Cheng, Adv. Mater. 22 (2010) E28.
[4] L. Chenguang, Yu Zhenning, N. David, A. Zhamu, B.Z. Jang, Nano Lett. 10 (2010) 4863.
[5] H. Wang, Y. Liang, T. Mirfakhrai, Z. Chen, H. Casalongue, H. Dai, Nano Res. 4 (2011) 729.
[6] J. Shaikh, R. Pawar, R. Devan, Y. Ma, P. Salvi, S. Kolekar, P. Patil, Electrochim. Acta 56 (2011) 2127.
[7] S. Chen, J. Zhu, X. Wu, Q. Han, X. Wang, ACS Nano 4 (2010) 2822.
[8] Y. Gao, S. Chen, D. Cao, G. Wang, J. Yin, J. Power Sources 195 (2010) 1757.
[9] J.P. Zheng, P.J. Cygan, T.R. Jow, J. Electrochem. Soc. 142 (1995) 2699.
[10] M. Min, K. MacHida, J. Jang, K. Naoi, J. Electrochem. Soc. 153 (2006) A334.
[11] B.J. Lee, S. Sivakkumar, J.M. Ko, J.H. Kim, S.M. Jo, D.Y. Kim, J. Power Sources 168 (2007) 546.
[12] S. Boukhalfa, K. Evanoff, G. Yushin, Energy Environ. Sci. 5 (2012) 6872.
[13] D. Choi, G. Blomgren, P. Kumta, Adv. Mater. 18 (2006) 1178.
[14] Z. LI, J. Tang, J. Yang, C. Cheng, Q. Xiao, G. Lei, Funct. Mater. Lett. 4 (2011) 61.
[15] Y.L. Cheah, N. Gupta, S.S. Pramana, V. Aravindan, G. Wee, M. Srinivasan, J. Power Sources 196 (2011) 6465.
[16] S.D. Perera, B. Patel, N. Nijem, K. Roodenko, O. Seitz, J.P. Ferraris, Y.J. Chabal, K.J. Balkus, Adv. Energy Mater. 1 (2011) 936.
[17] M. Roppolo, C. Jacobs, S. Upreti, N. Chernova, M. Whittingham, J. Mater. Sci. 43 (2008) 4742.
[18] S.D. Perera, B. Patel, J. Bonso, M. Grunewald, J.P. Ferraris, K.J. Balkus, ACS Appl. Mater. Interfaces 3 (2011) 4512.
[19] W.-C. Fang, W.-L. Fang, Chem. Commun. 41 (2008) 5236.
[20] Z. Chen, Y. Qin, D. Weng, Q. Xiao, Y. Peng, X. Wang, H. Li, F. Wei, Y. Lu, Adv. Funct. Mater. 19 (2009) 3420.
[21] C. Xiong, A.E. Aliev, B. Gnade, K.J. Balkus, ACS Nano 2 (2008) 293.
[22] Y. Wang, H. Zhang, W. Lim, J. Lin, C. Wong, J. Mater. Chem. 21 (2011) 2362.
[23] K. Takahashi, Y. Wang, G. Cao, Appl. Phys. Lett. 86 (2005) 1.
[24] G. Wee, H.Z. Soh, Y.L. Cheah, S.G. Mhaisalkar, M. Srinivasan, J. Mater. Chem. 20 (2010) 6720.
[25] H. Liu, W. Yang, Energy Environ. Sci. 4 (2011) 4000.
[26] X. Rui, J. Zhu, D. Sim, C. Xu, Y. Zeng, H.H. Hng, T.M. Lim, Q. Yan, Nanoscale 3 (2011) 4752.
[27] R. Amade, E. Jover, B. Caglar, T. Mutlu, E. Bertran, J. Power Sources 196 (2011) 5779.
[28] R.-R. Bi, X.-L. Wu, F.-F. Cao, L.-Y. Jiang, Y.-G. Guo, L.-J. Wan, J. Phys. Chem. C 114 (2010) 2448.
[29] Y. Sun, Q. Wu, G. Shi, Energy Environ. Sci. 4 (2011) 1113.
[30] J. Yoo, K. Balakrishnan, J. Huang, V. Meunier, B. Sumpter, A. Srivastava, M. Conway, A. Reddy, J. Yu, R. Vajtai, P. Ajayan, Nano Lett. 11 (2011) 1423.
[31] S.D. Perera, R.G. Mariano, K. Vu, N. Nour, O. Seitz, Y. Chabal, K.J. Balkus Jr., ACS Catal. 2 (2012) 949.
[32] G. Scheuermann, L. Rumi, P. Steurer, W. Bannwarth, R. Mülhaupt, J. Am. Chem. Soc. 131 (2009) 8262.
[33] L. Qu, Y. Liu, J.-B. Baek, L. Dai, ACS Nano 4 (2010) 1321.
[34] R. Cruz, T. Pacheco, A. Mendes, Solar Energy 86 (2012) 716.
[35] H. Kim, G. Moon, D. Monllor-Satoca, Y. Park, W. Choi, J. Phys. Chem. C 116 (2012) 1535.
[36] S.D. Perera, R.G. Mariano, N. Nijem, Y. Chabal, J.P. Ferraris, K.J. Balkus Jr., J. Power Sources 215 (2012) 1.
[37] J. Yanga, C. Zang, L. Sun, N. Zhao, Y. Zhou, Adv. Mater. Res. 287 (2011) 2356.
[38] S. Park, J. An, J. Potts, A. Velamakanni, S. Murali, R. Ruoff, Carbon 49 (2011) 3019.
[39] S. Stankovich, D. Dikin, R. Piner, K. Kohlhaas, A. Kleinhammes, Y. Jia, Y. Wu, S. Nguyen, R. Ruoff, Carbon 45 (2007) 1558.
[40] C.-Y. Su, Y. Xu, W. Zhang, J. Zhao, A. Liu, X. Tang, C.-H. Tsai, Yizhong Huang, L.-J. Li, ACS Nano 4 (2010) 5285.
[41] X. Zhou, J. Zheng, H. Wu, H. Yang, J. Zhang, S. Guo, J. Phys. Chem. C 115 (2011) 11957.
[42] V. Mohan, B. Hu, W. Qiu, W. Chen, J. Appl. Electrochem. 39 (2009) 2001.
[43] W. Avansi Jr., C. Ribeiro, E.R. Leite, V.R. Mastelaro, Cryst. Growth Des. 9 (2009) 3626.
[44] G.-M. Wu, A.-R. Wang, M.-X. Zhang, H.-Y. Yang, B. Zhou, J. Shen, J. Sol-Gel Sci. Technol. 46 (2008) 79.
[45] B. Yan, L. Liao, Y. You, X. Xu, Z. Zheng, Z. Shen, J. Ma, L. Tong, T. Yu, Adv. Mater. 21 (2009) 2436.
[46] W. Fang, J. Phys. Chem. C 112 (2008) 11552.
[47] R. Baddour-Hadjean, J.P. Pereira-Ramos, C. Navone, M. Smirnov, Chem. Mater. 20 (2008) 1916.
[48] T. Tsukamoto, K. Yamazaki, H. Komurasaki, T. Ogino, J. Phys. Chem. C 116 (2012) 4732.
[49] A. Das, B. Chakraborty, A. Sood, Bull. Mater. Sci. 31 (2008) 579.
[50] Ś.J. Mrowiecka, V. Maurice, S. Zanna, L. Klein, P. Marcus, Electrochim. Acta 52 (2007) 5644.
[51] X. Lang, A. Hirata, T. Fujita, M. Chen, Nat. Nanotechnol. 6 (2011) 232.
[52] H. Liu, Y. Wang, H. Li, W. Yang, H. Zhou, Chem. Phys. Chem. 11 (2010) 3273.
[53] L.-M. Chen, Q.-Y. Lai, Y.-J. Hao, Y. Zhao, X.-Y. Ji, J. Alloys Compd. 467 (2009) 465.
[54] K. Hung, C. Masarapu, T. Ko, B. Wei, J. Power Sources 193 (2009) 944.
[55] W. Xing, J.R. Dahn, J. Electrochem. Soc. 144 (1997) 1195.